Desalination and Water Treatment
www.deswater.com
doi: 10.5004/dwt.2021.26967

218 (2021) 177–192
April

Interplay of graphene oxide and interfacial polymerized polyamide-crosslinked thin-film composite membranes for enhanced performance during reverse osmosis

Sanju Gupta[a,b,c,*], Brendan Evans[b,†]

[a]*Department of Chemistry and Biochemistry, The City College of New York-CUNY, 160 Convent Ave., New York, NY 10031, USA, email: sgup77@gmail.com (S. Gupta)*
[b]*Department of Physics and Astronomy, Western Kentucky University, 1906 College Heights Blvd., Bowling Green, KY 42101, USA, email: brendan.evans054@topper.wku.edu (B. Evans)*
[c]*Biotechnology Center, Western Kentucky University, 1906 College Heights Blvd., Bowling Green, KY 42101, USA*

Received 21 September 2020; Accepted 21 December 2020

ABSTRACT

Graphene oxide (GO) and its functionalized derivates are regarded as promising due to superior hydrophilicity, mechanical stability, and biocidal properties, which overcomes the inherent limitations of current polymer membranes. In this work, thin-film nanocomposite (TFNC) membranes with a thin polyamide (PA) active layer embedded in multifunctional poly tannic acid modified GO (here on, pTA-f-GO) through interfacial polymerization are developed as emergent reverse osmosis membranes with new multifunction. The introduction of varied GO loadings, that is, pTA-f-GOx, x = 0, 40, 80, 120, 200, and 500 μg mL^{-1}, provided a tunable chemical composition, hydrophilicity, surface, and physicochemical properties potentially reduce electrolyte concentration polarization determined following ion retention estimates. The surface morphology of membranes revealed Turin-like structures and complex intra- and inter-polymer chain crosslinking. The flow of water molecules (ultrafast permeability), efficient adsorption of charged species (mono vs. divalent ions preference), bactericidal ability, and chlorine resistance of membranes are reported. Briefly, the water flux is enhanced by 30% and salt rejection increased for divalent ions as compared with monovalent ion species and the optimized behavior is observed for nominal GO concentration, that is, pTA-f-GOx membranes with x = 80 and 120 μg mL^{-1}. The incorporation of optimal GO also contributed to significant chlorine resistance by 75% and bactericidal properties by 80%. This study overcomes the demand and supply gap of drinkable freshwater through nanotechnology-enabled graphene oxide-polymer TFNC membranes, display energy-efficient, and cost-effectiveness, which are invaluable for industrial plants.

Keywords: Graphene oxide; Interfacial polymerization; Reverse osmosis; Bactericidal; Chlorine resistance

1. Introduction

Water is the most precious resource (similar to food and air) and it is an indispensable component on this "blue" planet for sustaining life. Despite the Earth is covered with water by 72%, dwindling resources with global increase in demand for clean freshwater requires coordinated research and development efforts with re-consideration of energy-efficient water filtration technologies [1–3]. Nanofiltration (NF), reverse osmosis (RO) and the recent forward osmosis (FO) processes that utilize thin membranes are the effective strategies to achieve

* Corresponding author.
This work was performed while the corresponding author was at the Western Kentucky University.
Current address: Department of Chemistry and Biochemistry, The City College of New York-CUNY, 160 Convent Ave., New York, NY 10031, USA.

† The co-author is an undergraduate student researcher.

significant removal of undesired solutes and contaminants from unclean water [4]. Current water desalination plants primarily use RO technology for producing potable water demanded by the rapidly increasing world population [5–7]. RO is a pressure-driven process that requires applied pressure greater than the osmotic pressure by which pre-filtered saline water or water with unwanted impurities is forced through a semi-permeable membrane, selectively transporting single valent ions (Na^+, K^+; Z = 1) and water molecules while rejecting divalent ions (Ca^{2+}, Mg^{2+}, and Ba^{2+}; Z = 2), heavy Z elements or multivalent ions, dissolved organic compounds (DOC) and other micron-sized biological organisms, thus producing drinkable water safely and in a sustainable way [1,3,8–10]. Membrane-based separations play important roles in processing food, chemical-, and bio-pharmaceutical industries, and produce water with desirable qualities from a wide range of water sources (i.e., groundwater, brackish water, wastewater, and seawater). Current membranes for molecular separation are based on thin-film polymers (aromatic polyamide; PA, cellulose acetate; CA, polysulfone; PS) and ceramics that seem to contain several advantages such as good separation capability and wide pH tolerance [11,12]. However, their performance is inherently limited due to the hydrophobic rough surface of the formed PA layer destined to have permeability/selectivity trade-offs [2,8,13]. Additional demerits are weak tolerance to high temperatures, strong acidic/alkaline reagents, biofouling propensity [14,15], organic solvents leading to chemical instability, and chlorine resistance [16,17]. The biofouling is typically caused by micro-organisms that adhere to the membrane surface under experimental hydrodynamic conditions during RO filtration, augmented by the non-specific covalent interactions [18]. Such disadvantages inspire the development of novel conceptualization for fabricating desirable membranes that will offer better thermal and chemical stability, ion differentiation (selectivity), structurally stable (mechanically robust), scalability, reproducibility, bacterostasis, energy efficiency, and cost-effectiveness. As for withstanding exposure to chlorine and interaction with membranes surface, it largely depends upon the chemical composition of the surface. For instance, it is the chemical structure of diamine chemical units which is aromatic in PA membranes is prone to oxidation. Therefore, it is proposed to have tertiary aliphatic diamines as compared to secondary and tertiary cycloaliphatic since the former component is inactive toward oxidative chlorine besides aliphatic PA that reversibly reacts with chlorine to yield *N*-chlorinated amide resulting in inhibition or prevention of membranes degradation [19].

Graphene and graphene-related materials (GRM) have been confirmed as excellent membranes for molecular separation by themselves as well as their integration with polymers and other nanomaterials. It is ascribed to their atomic-level thinness, high mechanical strength, chemical inertness, and imperviousness to the atom as small as helium [2,8,20–25]. Molecular dynamic (MD) simulations, where nanopores were theorized on the monolayer graphene basal plane, demonstrated the permeation of water molecules while rejecting undesired substances proficiently [24]. One could make traditional monolayer graphene with controlled nanopore size (i.e., nano-porous graphene; NPG) membranes useful for desalination with higher flux than those of current RO membranes [24–26]. However, significant fabrication and technical challenges persist despite MD simulations and various experimental efforts. Thus, they are limited in manufacturing scalable organized nanopores, mechanical robustness, and hydrophilicity required for practical implementations. Therefore, strategic development of graphene-based membranes with the most desirable characteristics while tackling the above-mentioned challenges present viable alternatives [26–28]. Additionally, by incorporating inorganic nanoparticles (e.g., CeO_2, Ag_{NP}, TiO_2, SiO_2, and zeolite) and/or carbon-based nanomaterials (e.g., carbon nanotubes; CNTs, carbon-fibers) in a dense polymeric structure, thin-film nanocomposite (TFNC) membranes can secure desirable features including mass transportation, chemical resistance, and antimicrobial potential. Graphene oxide (GO), which is graphene nanosheets with oxygenated functional groups at the basal and edge planes, is a promising nanomaterial that overcomes limitations by virtue of superior hydrophilicity, mechanical stability, and antifouling character. Other important advantage includes bactericidal activity attributed to oxidative stress from reactive oxygen species (ROS), rupturing and killing by sharp and jagged edges and entrapment of bacterial cells [29]. GO is a pseudo-two-dimensional material with strong in-plane covalent bonding and weak interlayer contacts with hydrogen bonding due to intercalated water molecules. Thus, it shows great potential for water and other solvents processability and ultra-smooth surface that can form unique water-transportation channels [30–32].

Fabrication of nanocomposite membranes with GO nanosheets embedded in polymeric structures (polysulfone; PSF and polyamide; PA) showing improved water filtration and biocidal properties are reported [33–35]. However, direct incorporation of GO in polymer creates aggregation causing disturbance in porous membrane structure and degradation. This incompatibility in organic polymers decreases the degree of cross-linking in polymeric structures and affect membrane performance [36]. The desired homogeneous dispersion of nanoscale GO nanosheets in polymeric thin-film membrane largely depends upon pH and surface polarity. Embedding GO with polymer chains in a controlled manner provides the foundation for the production of next-generations of emergent and advanced RO membranes with intended multifunction. Therefore, functionalizing GO sheets with chemical moieties and organic polymers are widely proposed for fabrication of dense thin film membrane surfaces with chlorine resistance and anti-biofouling characteristics [37]. Moreover, some of these polymers containing dipolar ions known as "inner salts" are ideal hydrogen bond acceptors/contributors that bind water molecules and form protein repulsive hydration layers on the membrane surface thus reducing adhesion of organic and bio-organic residues as foulants [38]. Furthermore, there has been an explosion in research into the development of a universal environmental-friendly nanocoating using either catecholamine or polydopamine. For example, Sileika et al. [39] described the ability of polyphenols such as tannic acid (TA) to oxidatively polymerize thin films. Similarly, Ejima et al. [40] reported the development of TA coating using coordination complexes with ferric ions

which exhibited free radical scavenging and antibacterial properties. Compared to polydopamine, poly(tannic acid) [pTA] has commercial applications in anti-biofouling with bactericidal activity, which is exploited in this study.

As a result of addressing the challenges of RO technologies, thin-film nanocomposite (TFNC) membranes are fabricated via interfacial polymerization (IP) reaction [41] utilizing the formation of PA thin active layer in concomitant with introducing GO nanosheets, as high-performance (water flux and bactericidal efficiency without affecting the water desalination properties) next-generation membranes comprising GO/polymer interphases. This work utilized the polyethyleneimine (PEI) functionalized TA coated GO with varying concentrations in the organic and aqueous phase and deposition time for synthesis parameter optimization following statistical Taguchi (L_3) method [42,43]. In the functionalized GO, the TA chemically binds with GO and the PEI crosslinks with TA through amination as well as into a thin PA active layer. This cross-linking integrates the GO into forming TFNC, optimizes the mechanical toughness and chemical resistance demonstrated by the range of microstructural and surface property characterization and performance measurements. The results are discussed while addressing the following: Are these TFNC membranes scalable and perform reproducibly? How the physicochemical properties affect the desalination performance? What is the mechanism by which the membrane surface composition influences chlorine resistance and biocidal activities? We strongly believe this work opens up new innovations for TFNC membranes with other significant value propositions while prevailing industrial tradeoffs, bactericidal, and anti-fouling features.

2. Materials and methods

2.1. Preparation of incubation chamber and materials dispersion

The GO-polymer membranes synthesis begins with the production of several different solutions and dispersions. The commercial (poly)ethersulfones (PES) mesoporous membranes support (pore size 0.1 μm, 4.3 cm diameter, Sterlitech, USA) were treated with solutions and dispersions in a particular order for a certain amount of time for fabricating TFNC membranes. The GO was prepared using modified Hummers' method described elsewhere [44–46] and the concentrated GO dispersion of 2 mg mL^{-1} was prepared with deionized (DI) water [45,46] to create a dispersion of lower concentrations of 40, 80, 120, 200, and 500 μg mL^{-1}. Tannic acid (TA) dispersion in DI water was also produced at 2 mg mL^{-1}. We also prepared 50 ml dispersion at 2 wt.% of camphor sulfonic acid (CSA), *m*-phenylenediamine (MPD), and triethylamine (TEA), all in DI water. PEI was mixed with bicine solvent at 2 mg mL^{-1} and trimesoyl chloride (TMC) with hexane solvent was produced at 0.15 wt.%, both 50 mL. All of these chemicals were used as purchased from Sigma-Aldrich™ (St. Louis, MO). The custom-designed incubation apparatus used to develop the membranes was relatively inexpensive considering the quality of the fabricated membranes. It consisted of a rectangular 12 × 24 cm^2 piece of plexiglass and 12 × 12 cm^2 square rubber gasket material, which were cut out into 6 × 6 cm^2. For the rubber gasket, a doctor blade, or a pair of high-quality scissors was extremely helpful in cutting precise edges. The square rubber pieces were cut into circular shape gaskets that conform to support PES membrane shape and size. Therefore, rubber gaskets were cut to the inner diameter of 41 mm (4.1 cm) to ensure complete coverage with the gasket over the edges of the PES support.

2.2. Fabrication of TFNC membranes

GO nanosheets of varying concentration were functionalized with PEI and cross-linked with TA designated here as pTA-f-GOx (x = 0, 40, 80, 120, 200, and 500 μg mL^{-1}). The first step involved setting the 41 mm diameter PES support membranes active side facing up between a clean poly(methyl methacrylate) PMMA or plexiglass backing plate and neoprene rubber gasket. Then, we topped with a PMMA open bottom container to leave about one millimeter on all edges to ensure the whole membrane is covered properly. It may be helpful to press down the rubber gasket onto the PMMA using palm or the setup was clamped to hold in place. The seal formed by this rubber gasket should be observed by viewing the plexiglass from the bottom, looking for any gaps, or missing coverage of the membranes such that the reaction solution is exposed to the active surface only. Once the placement of the gasket is completed, the membranes were ready for material exposure and the deposition duration is imperative to the fabrication. Starting with GOx (x = 0, 40, 80, 120, 200, and 500 μg mL^{-1}), create a mix of 1.5 mL of GO and 1 mL of tannic acid (TA) for each membrane. We developed eight membranes of each GO concentration including a pristine membrane. The GO/TA mixture of 2.5 mL is squirted in the membrane center that spreads uniformly on the entire surface. Following this, a plexiglass square is placed on top of the rubber gasket (forming a sandwich) to conceal and protect the GO/TA mixture. All of the membranes were incubated for 30-45 min and then the GO/TA mixture was removed with care using a dedicated syringe and the membranes were allowed to dry for about 30 min–1 h. For the second stage in the fabrication process, 0.5 mL of CSA, MPD, and TEA each were mixed (using ultrasonication for 30 min) for every membrane and 1.5 mL of this mixture is poured slowly with a syringe on each membrane. This mixture remains on the membrane surface for a total of 5 min. After 5 min, we removed the excess solution using a syringe (tilted to get any excess fluid) before the surface was exposed to TMC solution in hexane for 1–1.5 min, promoting the creation of a thin dense PA layer through interfacial polymerization. The as-prepared membranes were rinsed with hexane and cured in a vacuum oven at low temperature 60°C–70°C for 5 min, brought to room temperature, soaked in DI water, and stored in a fridge before performance tests. Fig. 1 shows the procedure of interfacial polymerization reaction scheme revealing the chemical reaction (activation and inhibition) and formulation of pTA-f-GO nanosheets demonstrating the spatial structures consisting of dots and stripes besides optical micrographs of representative membranes.

2.3. Membrane characterization

The membrane surface was characterized to reveal surface charge, hydrophilicity, morphology, roughness, and

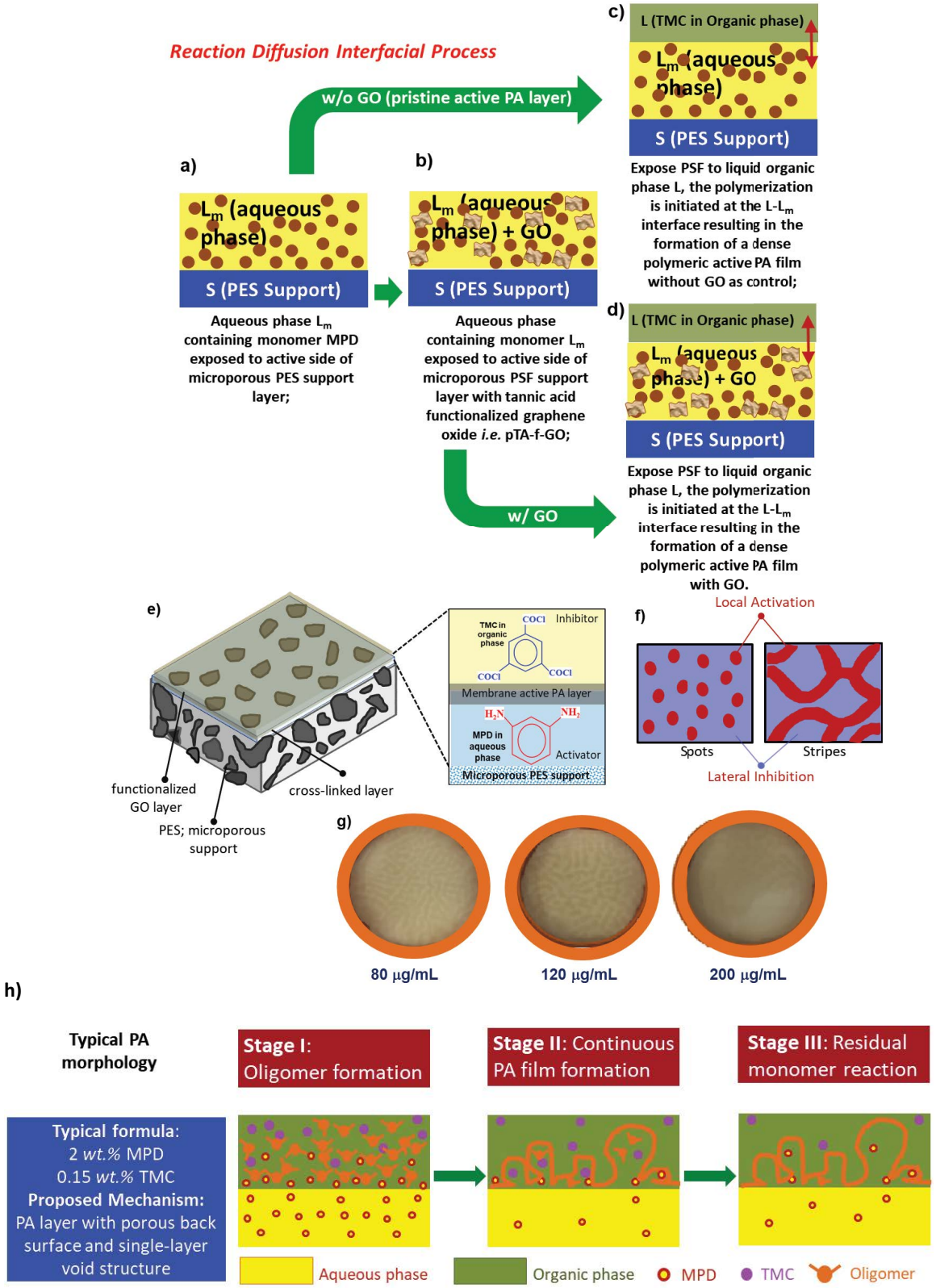

Fig. 1. (a–d) Schematic of interfacial polymerization reaction with and without GO. (e) The chemical reaction at the interface showing competing activation and inhibition kinetic pathways. (f) Spatial representation of Turing-like structures consisting of dots and stripes. (g) Optical micrographs of representative membranes with three different GO concentrations showing structures in real-time. The double-sided arrow (red) indicates the reactive site. (h) A cartoon of formation mechanism of PA thin active layer via interfacial polymerization on porous support membrane.

molecular surface properties using zeta potential, contact angle, scanning electron microscopy(SEM), atomic force microscopy (AFM), and Raman spectral measurements, respectively. The zeta potential (ζ) against pH were measured using an electrokinetic analyzer (Anton par, Graz, Austria) and for hydrophilicity, the contact angle was measured by taking air droplet images analyzed using OCA software [35]. SEM (model JSM-6510LV, MA) images were taken with electron acceleration voltage (V_{acc}) of 15 kV in secondary electron imaging (SEI) mode with LaB_6 filament. The topography of the membrane surfaces was also measured by AFM in non-contact mode via PicoPlus instrument (model series 5500, Molecular Imaging Inc., Ann Arbor, MI) in 5 × 5 μm² areas. Raman spectra were acquired using a micro-Raman spectrometer (model InVia Renishaw plc, Hoffman Estates, IL, USA) with laser excitation of wavelength 633 nm (or energy 1.92 eV). The scattered light is collected in backscattering geometry detected by Charged Coupled Device camera. An objective lens 50× gives rise to laser power on the sample maintained at <0.5 mW (5%) to avoid thermal degradation. Raman spectra ranged from 600 to 1,800 cm^{-1} with spectral resolution ~1 cm^{-1}.

2.4. RO setup for desalination performance, chlorine resistance tests, and correlated analysis

The membrane performance in terms of water permeation (permeability), salts ion, and organic probe dyes rejection (retention and adsorption), chlorine resistance, and bactericidal properties are evaluated. Their performance was measured using a commercial dead-end stirred filtration cell (Sterlitech, model UHP43, Kent, WA). The effective membrane area was ~14.5 cm^2 and all the experiments were performed at ambient temperature with applied pressure from 0.25 to 5 bar (2.5 to 60–65 psi or 413.7 kPa) using a nitrogen tank with a pressure regulator. The flux (L h^{-1} m^{-2}):

$$\phi = \frac{V_p}{t \cdot A} \text{ or} \tag{1}$$

permeability (L h^{-1} m^{-2} bar^{-1})

$$\chi = \frac{V_p}{t \cdot A \cdot \Delta P} \tag{2}$$

where V_p is the permeate volume, t is the permeation time, A is the membrane active area, and ΔP is the applied pressure, for RO water, salts, and organic probe dye solutions were determined after a constant flux was obtained. The procedure for flux/permeability, salt, and dye retention as well as cleaning was followed from our previous work on GO only membranes [8]. Briefly, to diminish the role of adsorption, the membranes were pre-saturated by filtering approximately 20–25 mL test solution, and then the membranes were washed with acetone followed by RO water. The retention performance of the membranes was evaluated by filling the cell with approximately 50–60 mL of solution and allowing 10 mL to permeate, which were collected and analyzed. All tests were repeated five times for reproducibility. For accurate estimation of the concentration of the probe dye molecules in the retentate, we rinsed all the cell components with RO water multiple times. The salt rejection was examined by using mono-(NaCl, KCl) and di-valent ($MgCl_2$, $CaCl_2$) electrolytes with a concentration of 0.5 g L^{-1}. To minimize the concentration polarization (CP) effect on the retention performance, the feed solution was occasionally stirred at 500 rpm during filtration. We begin the tests by recording the flux of RO water until a stable condition was achieved. Subsequently, RO water is replaced by approximately 50–60 mL of the salt solutions. The retention was calculated using:

$$R(\%) = \frac{C_f - C_p}{C_f} \times 100(\%) \tag{3}$$

where C_f is feed and C_p permeant concentration (mS cm^{-1}), respectively. The concentration of the salts was measured by a calibrated ion conductivity meter (Cole-Palmer, Oakton Instruments, model CON 450 meter, Vernon Hills, IL). Likewise, adsorption of organic probe dyes is calculated using:

$$\frac{V_f C_f - \left(V_r C_r + V_p C_p\right)}{V_f C_f} \times 100(\%) \tag{4}$$

where V_f, V_r, and V_p refer to the volume of feed, retentate, and permeate, respectively. The C_f for all the dyes used was 10 μM. Once all filtration was completed, we kept a ~1–2 mL amount of filtered R6G (Rhodamine 6G at ~500 nm; 116,000 M^{-1} cm^{-1}) and MB (Methylene Blue at 668 nm; 95,000 M^{-1} cm^{-1}) dyes to determine the concentration of permeate and retentate by optical absorption spectroscopy. A UV-vis spectrophotometer (Perkin-Elmer spectrophotometer, model 1050, Waltham, MA) in the range of 200–700 nm was used to determine the MB and R6G probe dyes permeate concentration. The estimates of CP values were determined following combined solution–diffusion/film model for solute transport in one-dimensional flow and a fully developed boundary layer [47]. Accordingly:

$$\text{CP} = \frac{C_m - C_p}{C_f - C_p} = \exp\left(\frac{J_s}{k}\right) \tag{5}$$

where C_m, C_p, and C_f are the concentration of solute at the membrane, of permeate and of feed solution, J_s is the flux of solute species, and k the mass transfer coefficient defined by D/δ, where δ is the boundary layer thickness. Alternatively, RO employs a membrane liquid separation process to reject dissolved solutes on a nanoscale level and the CP values can be estimated independent of concentration following rejection (R) behavior expressed as [48]:

$$\text{CP} = \frac{1 - R}{R} \tag{6}$$

The chlorine resistance was performed by exposing membranes to sodium hypochlorite (NaOCl) solution (3,000 ppm) for 2 h, prior to and post to repeating the RO water flux and NaCl rejection test [48]. All statistical analysis was performed using Origin software version 20.

One-way analysis of variance (ANOVA) was performed for comparison. The Levenberg–Marquardt algorithm as the least-squares method was used for statistical significance. Results were displayed as a mean of five replicates with *p*-value of 0.05.

2.5. Antibacterial properties of membranes

The bactericidal activity was quantitatively assessed against *Escherichia coli* (ATCC® 25922™, gram-negative strain) bacterial cells according to the live/dead test via measuring optical density (optical absorption at 600 nm; OD_{600}) that measures the survival/disintegration of *E. coli* cells. The bacterial culture which had been incubated in liquid Luria–Bertani (LB) media overnight at 37°C under shaking (180 rpm) was centrifuged at 4,000 rpm for 5 min. The obtained bacterial pellet was suspended in 20 mM phosphate buffer saline (PBS, pH 7.2). The working bacterial culture was prepared by amending the bacterial suspension in PBS with a final concentration of 0.2 mg mL^{-1} and incubation at 37°C under mild shaking (180 rpm). The bacterial density was about 10^7–10^8 CFU mL^{-1} (colony-forming unit or cells mL^{-1}). The bacterial suspension was diluted 100 times with PBS giving rise to working bacterial density at approximately 10^5 CFU mL^{-1}. A 300 μL of the diluted bacterial suspension was transferred and spread on the membranes and incubated at 37°C for 0 h and overnight (24 h) for CFU measurements albeit indirectly using optical density (method 1). CFU is a unit used to estimate the number of viable bacteria. The selected membranes were also soaked in saline solution (15 mL–0.85% (w/v)) after incubation time and vigorously shaken for 2 min and optical density was measured again (method 2). The biocidal efficiency of all the membranes was calculated using:

$$R\%_{OD600} = \frac{c_0 - c_{24}}{c_0} \times 100(\%) \quad (7)$$

where *R*% is the bacterial cell count reduction, c_0 and c_{24} are the optical density at 600 nm informally related to the bacteria count from culture immediately after inoculation (0 h) and after incubation for 24 h at membrane surface, respectively. The concentration is measured by UV-vis spectrophotometer (Perkin-Elmer, model 1050, Waltham, MA). We have also used SEM to demonstrate the deformation and disintegration of the bacterial cell walls on membranes surface with and without GO, the former is expected to inactivate bacterial microorganisms with only some fraction alive.

3. Results and discussion

3.1. Membrane characterization (surface charge, morphology, chemical microstructure of TFNC membranes surface with varying GO loading)

The zeta potential (ζ) is a measure of effective potential comprising the charged properties of the interrogated surface [49]. Fig. 2a shows the membranes tend to be positive for acidic solutions (pH ≤ 4.5) and transition to negative charge with increasing pH (pH ≥ 6.0), having isoelectric point in the pH range 4.3–6.0. Interestingly, all membranes

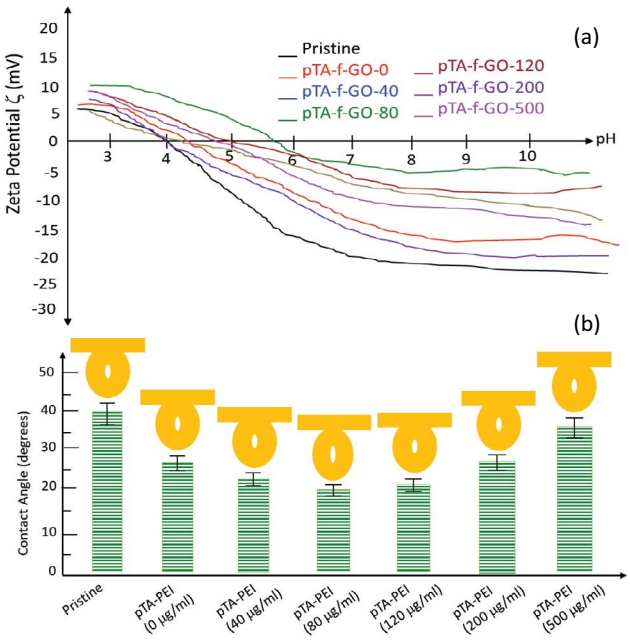

Fig. 2. (a) Zeta potential curves showing surface chemistry with pH and (b) contact angle in degrees for all the membranes.

except pTA-f-GO-80 and pTA-f-GO-120 have similar ζ behavior for pH ≤ 4.5. The zeta potential of the pristine membrane, that is, without GO and PES support membrane above pH 4.5 clearly has the most negative potential compared to all other membranes, attributed to the presence of free acid groups. This is in contrast to pTA membrane that has many phenolic and amine groups on the surface resulting in the less negative potential for pH > 4.5. While the surface charge for membranes with less GO (i.e., 80 and 120 μg mL^{-1}) has relatively less potential, the membranes without GO and other higher and lower GO concentrations are relatively same. Overall, the ζ value does not follow increasing GO loading trends, but it is the least negative for the medium GO concentration levels. According to the GO structure proposed by Lerf et al. [31], the carbons in GO contain two domains that are randomly distributed, aromatic regions with unoxidized benzene rings and aliphatic regions with six-membered carbon rings and relative domains size depends on the degree of oxidation. The phenolic hydroxyl groups along with carboxyl groups are responsible for the negatively charged surface of GO in aqueous suspension. The possible explanation of this behavior is the 80 μg mL^{-1} and possibly, 120 μg mL^{-1} loaded membranes that are optimally embedded in the polymer matrix and higher GO concentration is prone to aggregation. Further, oxidative interfacial polymerization chemistry of phenols is complex [50] that is aggrandized by the presence of PEI functionalized GO, where their relative contribution plays a vital role as far as the character of the final nanoscale coating is concerned. Typically, the ability of a hydrophilic surface to bind water molecules via electrostatic attractive forces creates a barrier at the interface leading to inhibition of foulant adhesion on membrane surface [35,51]. The pristine PES membrane has a contact angle

~44°, which decreases to 29° for the membrane without GO. Following the surface charge behavior with varying GO, the contact angle does not follow the trend with increasing GO loading. Instead, the behavior of contact angle follows the medium, low, and high GO with 25°, 20°, and 35° for the 40, 80, and 500 μg mL^{-1}, respectively, analogous to those of zeta potential behavior shown in Fig. 2b. Therefore, pTA-f-GO-80 membrane shows the most hydrophilicity supporting the hypothesis that the coating reaction is optimized by the effects of reduced interfacial energy between membrane surface and water molecules leading to higher water flux and expected membrane fouling discussed below.

Figs. 3a–f show SEM images revealing morphology of membranes surface with varying GO concentration. The characteristics such as surface irregularity or smoothness are important to filtration performance since the antifouling and bactericidal properties are affected by a decrease in efficiency of the hydrodynamic cleaning process and increasing binding sites [52,53]. The thick and rough ridge kind of morphology with micro-holes of a typical PES support and pTA functionalized membranes without GO is apparent as shown in Fig. 3a. The interfacial polymerization of pTA-PEI under ambient oxygen creates a layer of agglomerates that fill the valleys/micro-holes of the support structure resulting in a smoother surface. With GO introduction into the membrane coating, clear changes in morphology are observed. While surface coating with lower GO concentration pTA-f-GO-40 it was not sufficient to tailor the membrane morphology significantly, modification with a higher GO level from pTA-f-GO-120 onward results in the formation of GO nanosheet aggregation. Additionally, it is the medium GO level membrane pTA-f-GO-80 that creates a tighter and smoother PA active layer. It is noteworthy that the pTA-f-GO-80 membrane has relatively smoother surface topography as compared to pristine and without GO (pTA-f-GO-0) and therefore it is favorable for efficient performance. Qualitatively, the surface becomes rougher with increasing GO content indicative of aggregation, though low GO modified surfaces are relatively less rough than the pristine and higher GO membranes (Figs. 3g–j). Moreover, closer inspection of these membrane coatings reveals the spotted (lower GO) and striped (medium and higher GO) nanometer scale features, often known as turing-type structures, where the latter tend to have the larger surface area and generally consists of interconnected labyrinthine topography [54]. It is analogous to the Belousov–Zhabotinsky (BZ) microemulsion reaction consisting of reverse micelles [55]. An interfacial reaction between two chemical substances, namely, activator and inhibitor under certain conditions react and diffuse with each other (reaction–diffusion mechanism) generating spatiotemporal stationary structures [56], the shape of which can be manipulated by the well-controlled reaction occurring at the interface. It is demonstrated that the membranes with these Turin-type (bubble or tube) structures exhibit excellent desalination (water-salt | solvent-solute) performance surpassing an upper bound found with those of conventional membranes [57].

In general, interfacial polymerization (IP) is used to synthesize polymer particles, thin coatings, and membranes through step-growth reaction-diffusion mechanism taking place at the interface formed between two immiscible phases endowing unique topographical structures. Based on the polymerization kinetics during IP process, the growth rate and thereby polymer layer thickness depends upon the deposition time. Specifically, in the liquid monomer–solid (L_m–S) model useful for the current study (Figs. 1a–d, h), the polymerization reaction proceeds through diffusion at the reaction zone following kinetics from aqueous to organic phase following:

$$r = \frac{D}{\partial} K_{o/a} \phi_o C_m \tag{8}$$

where D is the diffusion coefficient in the membrane, ∂ is the reaction rate, r is the layer thickness, $K_{o/a}$ is the partition constant of the organic/aqueous phase at the interface, ϕ_o is the initial concentration of neutral monomer in the aqueous phase, and C_m is the total monomer concentration in the aqueous phase. Eventually, a thin PA active layer grows in the organic phase. Fig. 1h displays the scheme of the proposed three-step mechanism for the formation of PA thin active layer. The depleted morphological structure evolution is attributed to the variation in the distribution of MPD solubility in the interfacial reaction zone. The MPD in the aqueous phase have a greater tendency to diffuse faster into an organic phase containing TMC, which allows a higher polymerization rate and possibly the formation of a thicker active PA layer. In contrast, when low concentration GO of pTA-f-GO were incorporated into MPD aqueous phase, non-covalent interactions between the pTA-f-GO and MPD slows polymerization rate into the organic phase. Thus, there is a competing interaction wherein diffusion from the aqueous to organic phase becomes more significant as compared to the pristine case, which consumes more acid chloride groups of TMC and preventing cross-linking [58]. Beyond 40 μg mL^{-1} pTA-f-GO membranes increase crosslinking and active layer thickness with reduced hydrophilicity. Consequently, such membranes are expected to yield lower salt rejection and organic dyes adsorption. We found no systematic trend with GO for such behavior, instead of following a similar trend as for zeta potential and contact angle that is there is a demarcation in the behavior for pTA-f-GOx (x = 40, 120, 200, and 500) as compared to pTA-f-GOx (x = 80) membrane.

The three-dimensional surface topography and root mean square (rms) surface roughness (σ_{rms}) for pristine and with GO (pTA-f-GOx, x = 0, 80, 200, and 500 μg mL^{-1}) membranes are measured and provided in Fig. 3. The results show for high concentration pTA-f-GO (i.e., with 200 and 500 μg mL^{-1}) the membrane roughness is increased (Figs. 3i and j) as compared to pristine membrane (Fig. 3g). However, those utilizing medium concentration GO (i.e., with 80 and 120 μg mL^{-1}) the surface roughness was marginally larger than those of the highest GO concentration where the trend started to plateau (Fig. 3h). This may be due to well-dispersed GO nanosheets in the aqueous phase allowing the nanosheets to fill the voids for the pristine membrane making the lower concentration GO making the membrane surface smoother, while for medium concentration GO membranes surface were the roughest albeit marginally when compared with the highest GO concentration

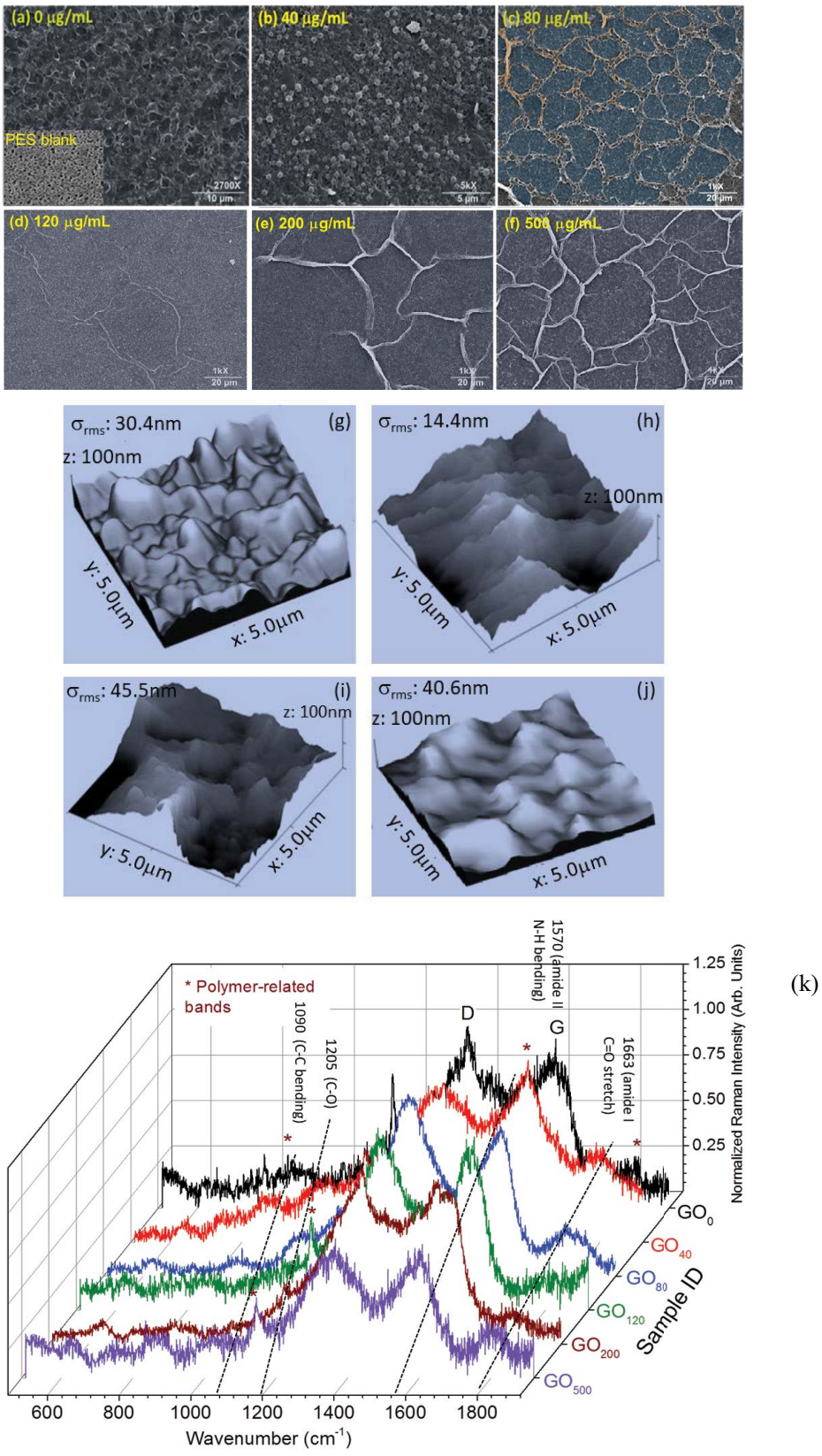

Fig. 3. (a–f) SEM images showing surface morphology. Scale bars is 5, 10, and 20 μm, (g–j) AFM images showing three-dimensional topography in 5 × 5 μm^2 region for pristine, 40, 80, and 500 μg mL^{-1} GO membranes, and (k) vibrational Raman spectra of membranes surface with varying GO.

membrane where the nanosheets tend to be parallel to the membrane surface partially due to aggregation. The average surface roughness (σ_{rms}) measured for pristine samples was 30.4 ± 2.7 nm and for the pTA-f-GO membranes with low, medium, and high GO the σ_{rms} values were 14.4 ± 1.2 (40 μg mL^{-1}), 45.5 ± 2.3 (80 μg mL^{-1}), 46.1 ± 1.5 (120 μg mL^{-1}), 42.6 ± 1.7 nm (200 μg mL^{-1}), and 40.6 ± 1.9 nm (500 μg mL^{-1}), respectively. Fig. 3k presents the micro-Raman spectral signatures identifying chemical composition of membrane surface with varying GO concentration. Typical, yet characteristic *D* (~1,340 cm^{-1}) and *G* (~1,608 cm^{-1}) bands for GO were observed assigned to the disorder activated and C–C stretching vibration, respectively. The peaks related to PA active layer in the pristine and other membranes include 1,663; 1,609; 1,205; 1,570; 1,205; and 1,090 cm^{-1} representing the amide I (C=O stretch), C=C stretching (overlaps with *G* band), amide II (N–H bending), C–O, and C–C bending, respectively, besides O–H band stretching between 3,000 and 3,500 cm^{-1} (not shown). Some of the lower wavenumber peaks get obscured due to the thinness of membrane and/or interaction reaction with the coating components. The 1,700 cm^{-1} peak is attributed to TA quinone groups and the broadness is due to the Schiff base (C=N) product formed between TA quinone groups and PEI. The basic lack of data variation with GO loading is due to the excitation wavelength penetration depth, that is, ~200–300 nm deeper than the coating thickness as well as sensitivity of the surface-sensitive Raman spectroscopy technique.

3.2. Evaluation of desalination performance of the membranes

The water flux (or permeability) and salt ion rejection (desalination) are two of the important factors defining membranes performance efficiencies besides underlying principle of hydrodynamics on surface discussed in this subsection. The TFNC membranes are evaluated by measuring the flow rate in a dead-end filtration cell with reverse osmosis water, four electrolyte salts, and two different organic probe dyes. The thinness of the PA active layer strongly suggests that these membranes are suitable for medium scale pressure-driven filtration. Figs. 4a–f summarizes the flux plots measured by filtering salt solutions (0.5 g L^{-1} or 500 mg L^{-1}) with applied pressure and the flux histograms (Fig. 4g) at the highest pressure of 60 psi. It is apparent that the flux through the membrane increases linearly with increasing applied pressure difference as expected. The results indicate that pristine membrane without GO (pTA-f-GO-0) was better than those of the higher GO membranes (pTA-f-GO-200 and pTA-f-GO-500) and the optimized GO concentration (pTA-f-GO-80) membrane was the most superior for alkaline or divalent ion (i.e., $CaCl_2$ and $MgCl_2$) electrolytes as compared to alkali or monovalent (i.e., NaCl and KCl) electrolytes. The RO technology which is pressure-driven process, the flux is proportional to the differential pressure or gradient in chemical potential following solution-diffusion model [59]:

$$\phi = A_w\left(\Delta\Pi - \Delta P\right) \tag{9}$$

where A_w is the permeability coefficient, $\Delta\Pi$ the osmotic pressure gradient, and P is the applied transmembrane pressure. It is clear that the applied pressure needs to overcome the osmotic pressure for a finite flux output. The departure of experimentally measured flux from classical linear behavior suggests that the velocity of the liquid flow at membrane surfaces is not zero. Such a fast transport of water and salt solutions is ascribed to: (1) low friction between water and exposed hydrophilic GO nanowalls and (2) ordered hydrogen bonds formed by the polymer active layer with GO functional groups to address water molecules being registered. The proportionality coefficient, A_w, is determined by fitting the linear part of the flux behavior. Water permeation (not shown), permeability coefficient (Fig. 4h) and salt rejection (or retention) determined from Eq. (3) for all the membranes investigated are summarized in Fig. 5 besides concentration polarization estimates from Eq. (6). The flux of the modified membrane with 80 μg mL^{-1} GO was improved by ~25% relative to the unmodified membrane. The salt rejection is influenced by the pTA-f-GOx membranes compared to the pristine membrane and follows similar trend as to surface charge and hydrophilicity behavior. In addition, it is effective toward divalent salt electrolytes by almost 10% as shown in Fig. 5. This finding is in compliance with those of surface charge and water contact angle analyses, where this particular membrane with optimized GO loading led to the most hydrophilic surface compared to the pristine, lower, and higher than 80 μg mL^{-1} of GO membranes. The improvements in salt rejection is attributed to the enhancement of the physicochemical (reasonably negatively charged and hydrophilic surface) properties of the dense and smoother thin PA active layer. These findings allow the fabricated nanocomposite membranes to overcome the trade-offs among permeation, salt rejection, and ion selectivity. Computer simulation shows that a graphene membrane containing nanopores/nanochannels lined with oxygenated groups, such as in our membranes, can trap cations in salt solutions under certain conditions and transport water molecules without much retardation. Similar observations have been made in atomically symmetric ultra-narrow nanopores in monolayer transition metal dichalcogenides (molybdenum disulfide, MoS_2) and hexagonal boron nitride (h-BN) [18]. The concentration polarization (CP) is an undesirable phenomenon since it exposes the membrane surface to an enhanced solute concentration which tends to decrease permeate flux by reduction of the pressure driving force through the increase in the counteracting osmotic pressure [48]. Following a combined solution–diffusion/film model and relating CP to R, we determined the estimates of CP for all of our membranes ranged between 8% and 25%. The membranes with optimal GO loadings (80 and 120 μg mL^{-1}) showed the lowest CP values, which is encouraging. Certainly, there appears to be a subtle interplay between Gibbs–Donnan equilibrium and adsorption equilibrium leading to non-monotonic variation of the ejection force to multivalent (or divalent in this study) salt concentration, which is in semi-qualitative agreement with experimental observations [60].

Now turning our attention toward the retention of organic probe dyes, the adsorption (Ads.) of organic dyes (methyl blue – MB, negatively charged and rhodamine 6G-R6G, electroneutral at pH = 6) is determined from UV-visible absorption spectroscopy calculated using Eq. (4).

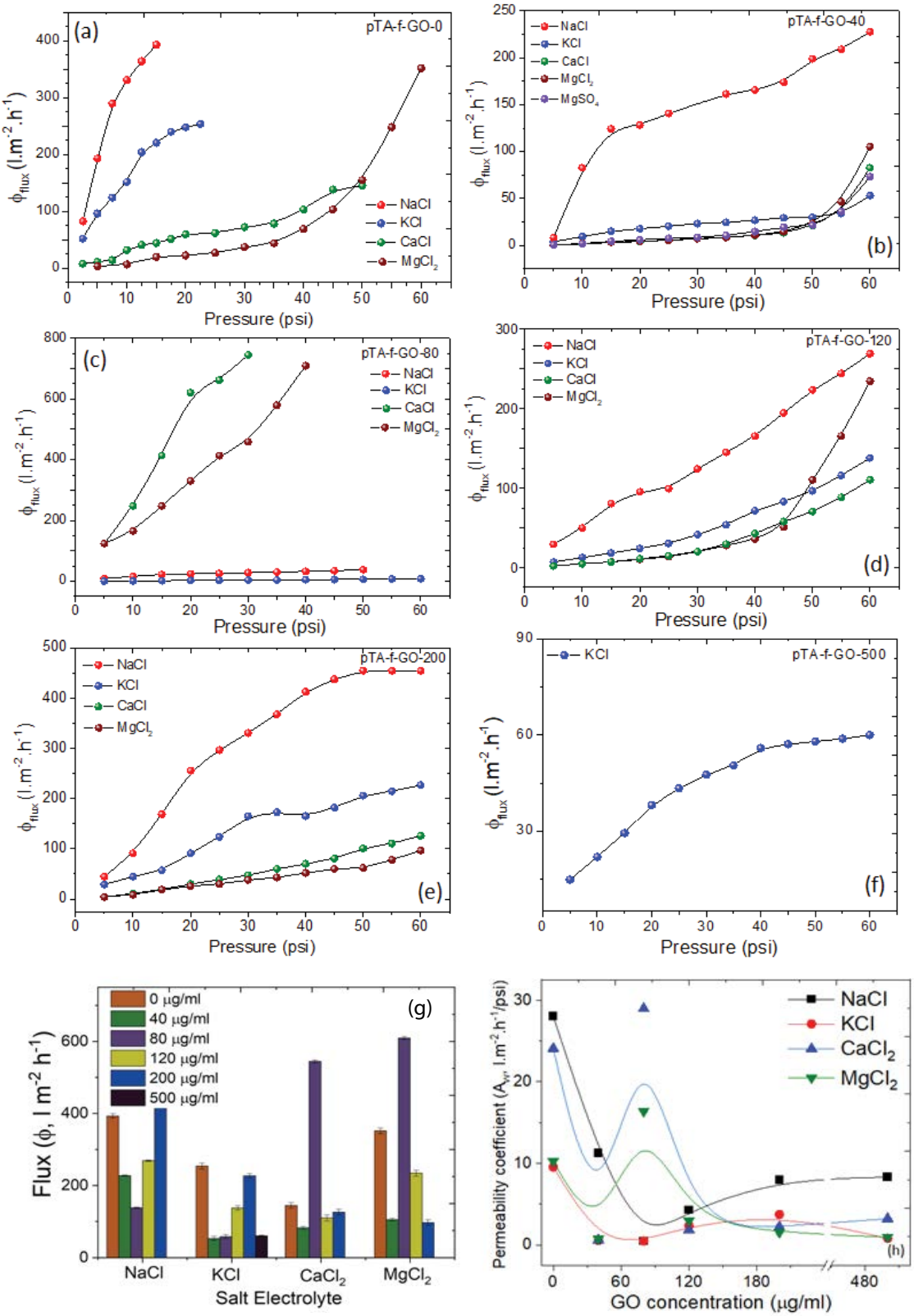

Fig. 4. Filtration performance (a–f) flux (ϕ) with applied pressure of alkali and alkaline salts for membranes with histograms at the maximum applied pressure difference and GO loadings. (g) Flux histograms at the maximum applied pressure difference. Error bars are from five measurements showing the maximum and minimum values. (h) Membrane permeability coefficient (Aw) determined from (a–f).

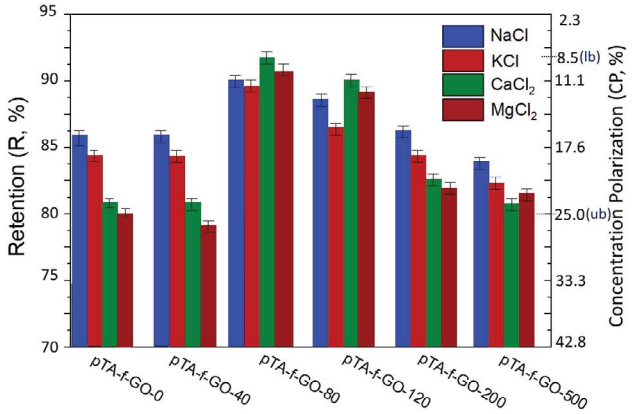

Fig. 5. Various salts retention or rejection (*R*, %) histograms of the membranes with varying GO loading. The estimated concentration polarization (CP, %) values are on the right ordinate axis showing lower (lb) and upper bound (ub). Error bars are from five measurements.

They exhibited high retention (~90%) for charged (MB) and uncharged (R6G) molecular probes comparably with solvation radius ~5Å. Based on these measurements, it appears that the membranes physically entrap molecules comparable to the size of probe dye molecules, reported as hydrated radii (~5Å) mentioned above. It is worth noting that the negatively charged probe molecules have marginally larger retention than the positively charged and neutral molecules suggestive of electrostatic repulsion.

3.3. Influences of pTA-f-GO incorporation on chlorine resistant and bactericidal characteristics of membranes

Chlorine is a common oxidizing biocide agent used for water disinfection. It is also used in RO treatment process to control the adhesion of biological micro-organisms that bio-foul the membranes during water purification and treatment. Therefore, chlorine-resistant polymeric membranes are highly desirable that can withstand exposure to chlorine and while preserving their separation characteristics under such harsh condition. While current aromatic PA membranes are limited in operating pH range (4–7), susceptibility to biological attack, and structural degradation under high pressure during RO process, the PA thin film composite (TFC) membranes feature desirable properties. Nevertheless, nanotechnology-enabled membranes by virtue of functionalized GO impregnation within the polymeric thin layer matrix adds a bonus for the desalination industry. Here in this subsection, we demonstrate the anti-chlorine and biocidal performances of the strategically synthesized TFNC membranes. The variation in flux of RO water and NaCl for chlorinated (used) and non-chlorinated (unused) membranes is summarized in Fig. 7. The flux varies linearly as anticipated with the highest flux for pTA-f-GO-80 membrane followed by comparable results for pTA-f-GO-40 and pTA-f-GO-120 membranes under non-chlorinated and post-chlorination treatment. Generally speaking, the water flux and salt rejection with the embedded GO in the thin PA active layer are higher than those of the pristine membrane.

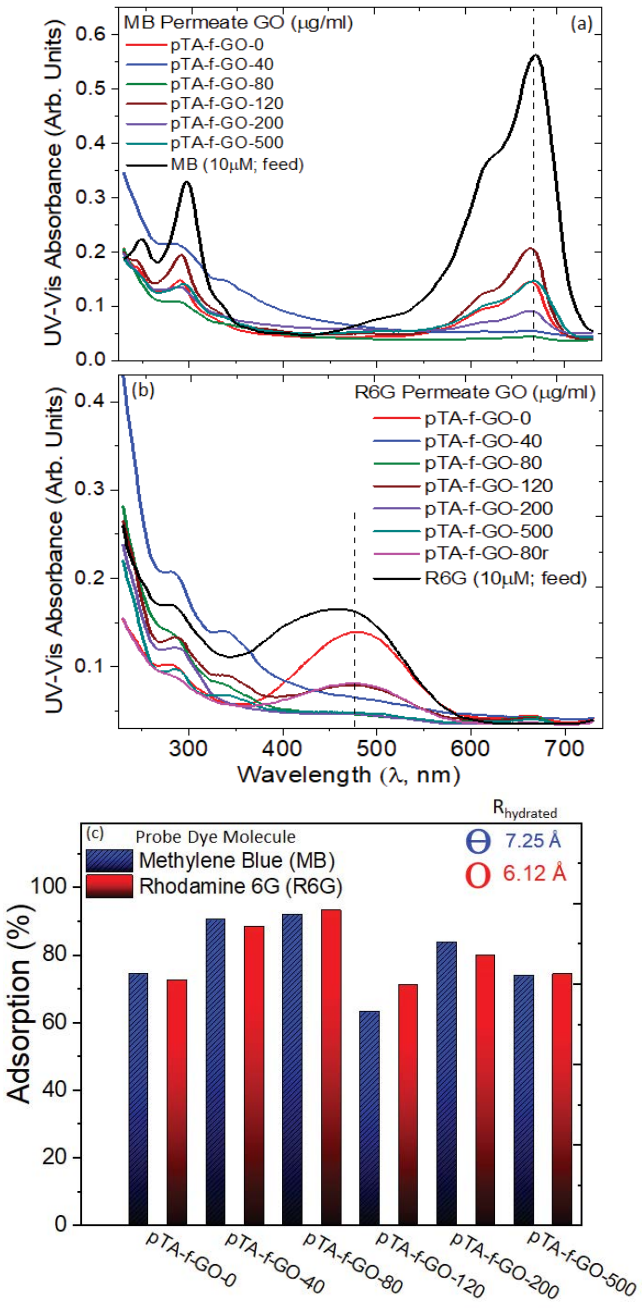

Fig. 6. (a and b) UV-visible absorption spectra of the organic probe dyes (MB and R6G) permeate solution from different membranes along with feed solution (10 μM). (c) Adsorption (or removal) histograms of MB and R6G dyes of different membranes. The blue and red symbols represent negatively charged and electroneutral organic probe dyes with their hydrated molecular size, respectively.

Quantitatively, water flux increased from approximately 400 to 750 L m^{-2} h^{-1} in contrast to the pristine membrane where salt rejection decreases marginally by 4% (Figs. 7a and b) attributed to the degradation of the PA active layer triggered by chemical attachment of chlorine [61]. Improved membrane performance with optimal loaded

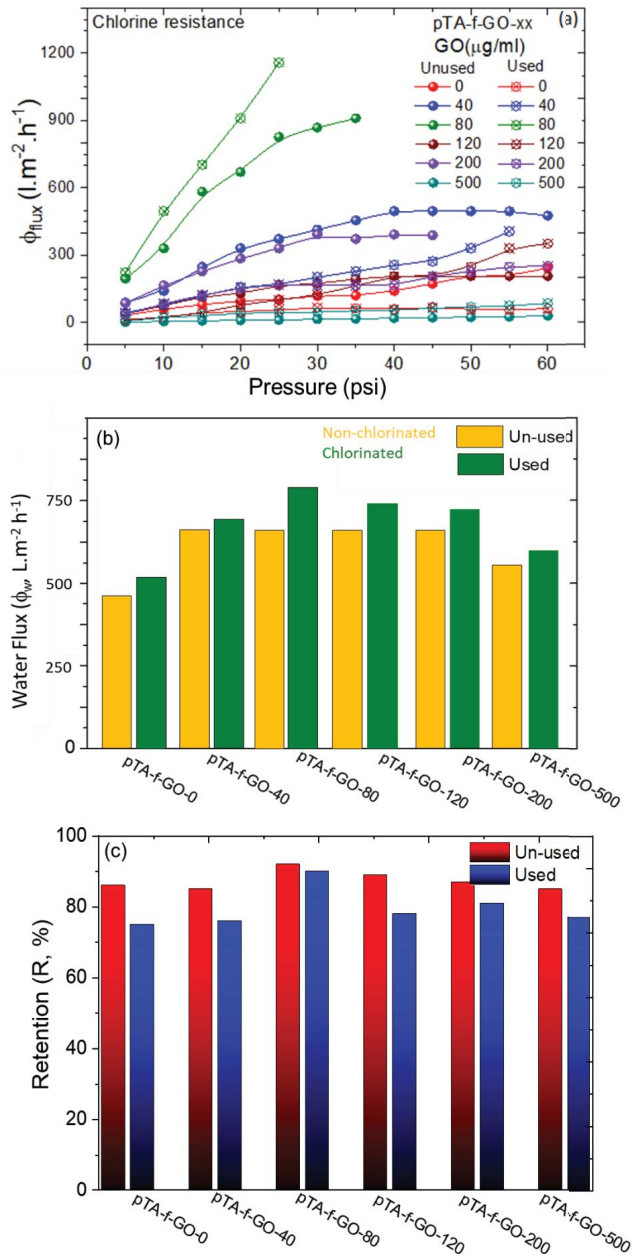

Fig. 7. Chlorine resistance performance (a) water flux (ϕ) with applied pressure, (b) water flux (ϕ) histograms at the maximum applied pressure difference, and (c) salt (NaCl) retention (*R*, %) histograms, for non-chlorinated (unused) and chlorinated (used) membranes, with varying GO loading.

GO is related to the intensive hydrogen bonding network introduced between pTA-f-GO and PA with significantly reduced aggregation in addition to the shielding of PA active layer by pTA-f-GO from chlorine degradation [62].

For the fundamental mechanism underpinning the interaction of chlorine with membrane surface constituents, amide nitrogen (–NH) is vulnerable to chlorine attack because of the electron-withdrawing effect of the carbonyl (C=O) group. Upon exposure, N–H group is chlorinated to N–Cl group which can reversibly form the initial amide by reducing agents. The aromatic rings are susceptible to attack by chlorine because it is an electron-rich region. When the characteristic aromatic polyamide (PA) layer is exposed to sodium hypochlorite (NaClO), it is ionized to produce hypochlorite ions according to the following reaction: $NaOCl \leftrightarrow Na^+ + ClO^-$. The established chlorinating strength is in the order of NaOCl and ClO^-. To enhance chlorine resistance of PA layer, adding protective groups at the possible chlorination sites on the aromatic rings is recommended. Additionally, while polysulfone has better chlorine resistance due to stronger chemical bonds, but due to hydrophobic nature, introducing hydrophilic groups, for example, $-SO_3H$, while retaining its physical properties, is indispensable. To address such issues, the key solution was to introduce polymer functionalized GO in contact with PA that protects delicate RO membranes was adopted in this study.

Finally, we evaluate membranes in terms of bacterial exposure causing bactericidal activity with subsequent biofouling which is an undesired accumulation (and/or growth) of micro-organisms (biofilm formation). In particular, biofouling adversely impacts membrane filtration performance by an additional hydraulic resistance, reduction in apparent flux (permeability), ion retention, and higher feed channel pressure drop. Consequently, physical and chemical cleaning routines are periodically applied to reduce biofouling impacts on membranes making them expensive undertakings. The bactericidal properties of pristine and pTA-f-GO membranes are evaluated against *E. coli* bacterial cells on the membrane surface at zero time (0 h) and after 1 d (24 h) of contact by assessing morphology, structure, and semi-quantitative measure of live cells reduction using electron micrographs and optical density at 600 nm following Eq. (5), respectively. The as-prepared unwashed and washed bacterial cells on pristine and pTA-f-GO membranes surface were observed by SEM presented in Figs. 8a–t). In general, SEM images depicted a growing cluster of Gram-negative, rod-shaped morphology with regular and intact membranes of a pathogenic strain of *E. coli* bacteria. Also, whether direct interaction of bacteria and graphene oxide nanosheets containing polymeric PA thin active layer could exhibit a key role in the antibacterial activity is analyzed via morphological changes. It is evident from SEM images that reveal capturing of bacterial adsorption on the polymer functionalized GO that coats on the bacteria and cause cell membrane damage thus assisting in growth inhibition of bacteria. *E. coli* incubated on pTA-f-GO membranes exhibited severe deformation in cell shape with evident shrinkage probably due to collapse of the internal structure. In some cases, the outer membranes merged with those belonging to the other bacteria cells. *E. coli* cells when incubated with method 2, it also exhibited similar behavior. The only difference between the method 1 (without) and method 2 (with) lies in the membrane treatment of in the latter with a concentrated saline solution followed by measuring the bacterial cell optical density from the membrane surface post 24 h incubation. The pTA-f-GO membrane samples displayed high bacterial inactivity of 75% reduction in the bacterial colonies compared to the pristine membrane, with the pTA-f-GO-80 (and pTA-f-GO-120) membrane yielding the highest antibacterial ability (~80%) especially post-saline treatment. The measure of

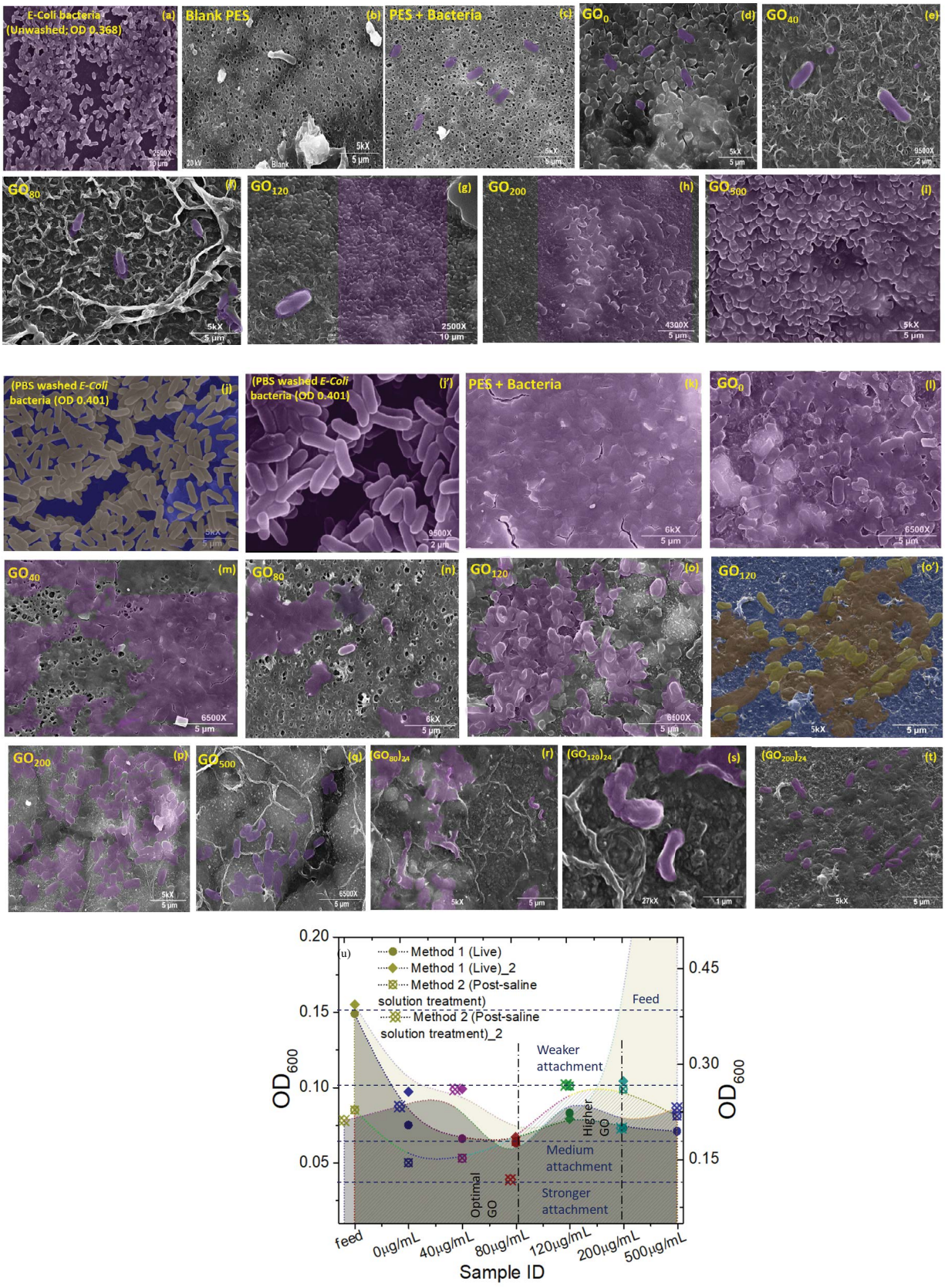

Fig. 8. SEM micrographs of (a–i) dead and (j–t) live *E. coli* bacterial cell activity at 0 h and after 24 h. (u) Antibacterial (or biocidal) activity variation for live bacteria in terms of optical density at 600 nm (OD_{600}) of the membranes as a function of GO nanosheet loading.

OD at 600 nm plotted in Fig. 8u is indicative of live or conversely dead (disintegrated and deformed) bacterial cells. The experimental results could be explained by synergistic effects among the presence of ROS facilitated by commonly attributed oxidative stress enabled by functionalized GO (oxygenated functional groups at the edges and in the basal plane) and with polymer chain leading to inhibited growth of bacteria, the toxicity, antibacterial activity, and cell membrane damage by lipid peroxidation [49,63]. In addition to these commonly proposed mechanisms, other mechanisms such as electron transfer in negatively charged *E. coli* bacterial membrane to significantly less negatively charged GO and NaCl treated membranes surface may result in ROS-independent oxidative stress [64], cell membrane damage by lipid peroxidation and mechanical tearing of cell membrane depending on the protruded sharp edges of GO nanosheets [49,65], as well as phosphate starvation [66], are proposed. The experimental findings are apparently supported by the capturing and killing mechanisms influencing higher biocidal effect for pTA-f-GO membranes [67]. In fact, a similar approach is typically adopted for concentrating bacteria and other micro-organisms while detecting and quantifying pathogens in water [68].

All of these findings demonstrate that incorporating polymer-decorated GO in the polyamide thin active layer is a promising method to fabricate nanocomposite membranes with improved performance such as chlorine resistance and anti-biofouling. This study overcomes the gap between demand and supply of producing potable freshwater through nanotechnology-enabled scalable graphene-polymer membranes, resulting in energy-efficient and increased cost-effectiveness, for direct industrial and biomedical applications.

4. Summary

The production of clean water using RO technology in an effective and energy-efficient manner requires strategic synthesis of membranes that overcome industrial trade-offs among water permeability (flux), salt retention (rejection), ion selectivity, concomitant with chlorine resistance, bactericidal properties, and structural robustness. In this study, the strategic development of scalable TFNC membranes with an embedded thin and dense polyamide active layer loaded with graphene oxide nanosheets via interfacial polymerization are investigated as efficient membranes including anti-chlorine and anti-bacterial characteristics. The addition of a small amount of graphene-based nanomaterial significantly improved the membranes physicochemical properties. The micro- and meso-scale structures showed Turin-like morphologies consisting of dots and stripes at reactive sites along with in-between inhibiting regions, which started to become uniform with increasing GO concentration. Additionally, the membranes showed reasonable surface charge and hydrophilicity with optimal GO concentration as compared to the control, pristine, lower, and higher GO loaded TFNC membranes. The pTA-f-GO-80 nanocomposite membrane exhibited the salt retention in the following increasing order: $R_{NaCl} \cong R_{KCl} < R_{CaCl_2} < R_{MgCl_2}$. These values are somewhat lower than those of commercial desalination nanofiltration membranes with an average of 8% and 12% improvements in the rejection of monovalent and divalent ions, respectively.

With improved water affinity and negative surface charge, the pTA-f-GO-80 membrane resisted chlorine degradation and intensify bacterial attachment, with ~75%–80% reduction in cell density as compared to the control, lower and higher GO of 30% and 50%, respectively. Overall, the potential of GO loaded novel nanocomposite membranes by facile method is promising as they retain many of the exceptionally tailored physicochemical properties of dense polymer layer offering greater flexibility besides elucidation of enhanced perm-selectivity, anti-chlorine, and biocidal activities. Additionally, these membranes are energy-efficient for the clean water production industry thereby can relieve the stress of water scarcity as well as biomedical use where antifouling coatings are intensely desired.

Authorship contributions

SG: conceptualization, investigation, acquisition of *E. coli* bacteria suspension (dead and live) source, data curation, supervision, funding acquisition, resources, writing – original draft. BE: investigation, data curation, experimental subsection first draft.

Acknowledgments

The author (SG) gratefully acknowledges financial support in parts by KY NSF EPSCoR REG (subaward# 323200000271-18-059), KY NSF EPSCoR RSP (subaward# 3200000271-17-212), NSF-MRI (Grant# 1429563) grants and internal RCAP award. The author (BE) is thankful to KY NSF EPSCoR RSP (subaward# 3200000271-17-212) for student research scholarship. The authors (SG and BE) are grateful to Naomi Rowland and John Andersland, both from Biology for providing cultured bacterial cells and for SEM training, respectively. Finally, we would like to thank the referee for careful reading of this manuscript.

References

[1] M.A. Shannon, P.W. Bohn, M. Elimelech, J.G. Georgiadis, B.J. Marinas, A.M. Mayes, Science and technology for water purification in the coming decades, Nature, 452 (2008) 301–310.
[2] L. Huang, M. Zhang, C. Li, G. Shi, Graphene-based membranes for molecular separation, J. Phys. Chem. Lett., 6 (2015) 2806-2815.
[3] M. Hu, B. Mi, Enabling graphene oxide nanosheets as water separation membranes, Environ. Sci. Technol., 47 (2013) 3715-3723.
[4] T. Basile, A. Petrella, M. Petrella, G. Boghetich, V. Petruzzelli, S. Colasuonno, D. Petruzzelli, Review of endocrine-disrupting-compound removal technologies in water and wastewater treatment plants: an EU perspective, Ind. Eng. Chem. Res., 50 (2011) 8389-8401.
[5] F. Perreault, A.F. de Faria, M. Elimelech, Environmental applications of graphene-based nanomaterials, Chem. Soc. Rev., 44 (2015) 5861-5896.
[6] D. Chohen-Tanugi, J.C. Grossman, Mechanical strength of nanoporous graphene as a desalination membrane, Nano Lett., 14 (2014) 6171-6178.
[7] L.F. Greenlee, D.F. Lawler, B.D. Freeman, B. Marrot, P. Moulin, Reverse osmosis desalination: water sources, technology, and today's challenges, Water Res., 43 (2009) 2317-2348.

[8] S. Gupta, A. Henson, B. Evans, Novel formulations for scalable multilayer nanoporous graphene-based membranes for use in efficient water detoxification revisited, Desal. Water Treat., 169 (2019) 59-71.
[9] S. Garaj, S. Liu, J.A. Golovchenko, D. Branton, Molecule-hugging graphene nanopores, Proc. Natl. Acad. Sci. U.S.A., 110 (2013) 12192-12196.
[10] M. Elimelech, The global challenge for adequate and safe water, J. Water Supply Res. Technol. AQUA, 55 (2006) 3-10.
[11] M.M. Pendergast, E.M.V. Hoek, A review of water treatment membrane nanotechnologies, Energy Environ. Sci., 4 (2011) 1946-1971.
[12] G.M. Geise, H.S. Lee, D.J. Miller, B.D. Freeman, J.E. McGrath, D.R. Paul, Water purification by membranes: the role of polymer science, J. Polym. Sci., Part B: Polym. Phys., 48 (2010) 1685–1718.
[13] D. Rana, T. Matsuura, Surface modification for antifouling membrane, Chem. Rev., 110 (2010) 2448-2471.
[14] B. Mi, M. Elimelech, Silica scaling and scaling reversibility in forward osmosis, Desalination, 312 (2013) 75-81.
[15] C. Liu, K. Rainwater, L.F. Song, Energy analysis and efficiency assessment of reverse osmosis desalination process, Desalination, 276 (2011) 1736-1744.
[16] J.E. Gu, B.M. Jun, Y.N. Kwon, Effect of chlorination condition and permeability of chlorine species on the chlorination of a polyamide membrane, Water Res., 46 (2012) 5389-5400.
[17] P. Marchetti, M.F. Solomon Jimenez, G. Szelesky, A.G. Livingston, Molecular separation with organic solvent nanofiltration: a critical review, Chem. Rev., 114 (2014) 10735-10806.
[18] R.A. Al-Juboori, T. Yusaf, Biofouling in RO system: mechanisms, monitoring and controlling, Desalination, 302 (2012) 1-23.
[19] K. Hashiba, S. Nakai, M. Ohno, W. Nishijima, T. Gotoh, T. Iizawa, Deterioration mechanism of a tertiary polyamide reverse osmosis membrane by hypochlorite, Environ. Sci. Technol., 53 (2019) 9109–9117.
[20] S.P. Surwade, S.N. Smirnov, I.V. Vlassiouk, R.R. Unocic, G.M. Veith, S. Dai, S.M. Mahurin, Water desalination using nanoporous single-layer graphene, Nature Nanotechnol., 10 (2015) 459-464.
[21] S. Gupta, A. Henson, B. Evans, R. Meek, Graphene-based aerogels with carbon nanotubes as ultrahigh-performing mesoporous capacitive deionization electrodes for brackish and seawater desalination, Desal. Water Treat., 162 (2019) 97-111.
[22] M.L. Hidalgo, S. Hu, O. Marshall, A. Mishchenko, A.N. Grigorenko, R.A.W. Dryfe, B. Radha, I.V. Grigorieva, A.K. Geim, Sieving hydrogen isotopes through two-dimensional crystals, Science, 351 (2016) 68-70.
[23] D. Konatham, J. Yu, T.A. Ho, A. Striolo, Simulation insights for graphene-based desalination membranes, Langmuir, 29 (2013) 11884-11897.
[24] D.C. Tanugi, L.-C. Lin, J.C. Grossman, Multilayer nanoporous graphene membranes for water desalination, Nano Lett., 16 (2016) 1027-1033.
[25] D.M. Stevens, J.Y. Shu, M. Reichert, A. Roy, Next-generation nanoporous materials: progress and prospects for reverse osmosis and nanofiltration, Ind. Eng. Chem. Res., 56 (2017) 10526-10551.
[26] A. Nicolai, B.G. Sumpter, V. Meunier, Tunable water desalination across graphene oxide framework membranes, Phys. Chem. Chem. Phys., 16 (2014) 8646-8654.
[27] R.K. Joshi, P. Carbone, F.C. Wang, V.G. Kravets, Y. Su, I.V. Grigoriev, H.A. Wu, A.K. Geim, R.R. Nair, Precise and ultrafast molecular sieving through graphene oxide membranes, Science, 343 (2014) 752-754.
[28] W.F. Chan, E. Marand, S.M. Martin, Novel zwitterion functionalized carbon nanotube nanocomposite membranes for improved RO performance and surface anti-fouling resistance, J. Membr. Sci., 509 (2019) 166-175.
[29] S.R.-V. Castrillón, F. Perreault, A.F. de Faria, M. Elimelech, Interaction of graphene oxide with bacterial cell membranes: insights from force spectroscopy, Environ. Sci. Technol. Lett., 2 (2015) 112-117.
[30] W. Scholz, H.P. Boehm, Untersuchungen am Graphitoxid. VI. Betrachtungen zur Struktur des Graphitoxids, Z. Anorg. Allg. Chem., 369 (1969) 327-340.
[31] A. Lerf, H. He, M. Forster, J. Klinowski, Structure of graphite oxide revisited, J. Phys. Chem. B, 102 (1998) 4477-4482.
[32] S. Dervin, D.D. Dionysiou, S.C. Pillai, 2D nanostructures for water purification: graphene and beyond, Nanoscale, 8 (2016) 15115-15131.
[33] B.M. Ganesh, A.M. Isloor, A.F. Ismail, Enhanced hydrophilicity and salt rejection study of graphene oxide-polysulfone mixed matrix membrane, Desalination, 313 (2013) 199-207.
[34] S. Bano, A. Mahmood, S.-J. Kim, K.-H. Lee, Graphene oxide modified polyamide nanofiltration membrane with improved flux and antifouling properties, J. Mater. Chem. A, 3 (2015) 2065-2071.
[35] H.M. Hegab, A. El Mekawy, T.G. Barclay, A. Michelmore, L. Zou, D. Losic, C.P. Saint, M.G. Markovic, A novel fabrication approach for multifunctional graphene-based thin film nanocomposite membranes with enhanced desalination and antibacterial characteristics, Sci. Rep., 7 (2017) 1-10.
[36] Y.P. Tang, J.X. Chan, T.S. Chung, M. Weber, C. Staudt, C. Maletzko, Simultaneously covalent and ionic bridging towards antifouling of GO-imbedded nanocomposite hollow fiber membranes, J. Mater. Chem. A, 3 (2015) 10573-10584.
[37] P.B. Lutz, E. Converse, P. Cebe, A. Asatekin, Self-assembling zwitterionic copolymers as membrane selective layers with excellent fouling resistance: effect of zwitterion chemistry, ACS Appl. Mater. Interfaces, 9 (2017) 20859-20872.
[38] T. Tong, S. Zhao, C. Boo, S.M. Hashmi, M. Elimelech, Relating silica scaling in reverse osmosis to membrane surface properties, Environ. Sci. Technol., 51 (2017) 4396-4406.
[39] T.S. Sileika, D.G. Barrett, R. Zhang, K.H.A. Lau, P.B. Messersmith, Colorless multifunctional coatings inspired by polyphenols founds in tea, chocolate, and wine, Angew. Chem. Int. Ed., 52 (2013) 10766-10770.
[40] H. Ejima, J.J. Richardson, K. Liang, J.P. Best, M.P. van Koerverden, G.K. Such, J. Cui, F. Caruso, One-step assembly of coordination complexes for versatile film and particle engineering, Science, 341 (2013) 154-157.
[41] Y. Song, J.-B. Fan, S. Wang, Recent progress in interfacial polymerization, Mater. Chem. Front., 1 (2017) 1028-1040.
[42] A.C. Atkinson, A.N. Donev, R.D. Tobias, Optimum Experimental Designs, with SAS, Oxford University Press, Oxford, pp. 511+xvi.
[43] N. Logothetidis, H.P. Wynn, Quality through Design: Experimental design, Off-Line Quality Control, and Taguchi's Contributions, Oxford University Press, Oxford Science Publications, Oxford, pp. 464+xi.
[44] S.W. Hummers Jr., R.E. Offeman, Preparation of graphitic oxide, J. Am. Chem. Soc., 80 (1958) 1339-1339.
[45] D.C. Marcano, D.V. Kosynkin, J.M. Berlin, A. Sinitskii, Z. Sun, A. Slesarev, L.B.W. Lu, J.M. Tour, Improved synthesis of graphene oxide, ACS Nano, 4 (2010) 4806-4814.
[46] S. Gupta, A. Irihamye, Probing the nature of electron transfer in metalloproteins on graphene-family materials as nanobiocatalytic scaffold using electrochemistry, AIP Adv., 5 (2015) 037106-1–037106-15, doi: 10.1063/1.4914186.
[47] I. Sutzkover, D. Hasson, R. Semiat, Simple technique for measuring the concentration polarization level in a reverse osmosis system, Desalination, 131 (2000) 117–127.
[48] S.G. Kim, D.H. Hyeon, J.H. Chun, B.-H. Chun, S.H. Kim, Novel thin nanocomposite RO membranes for chlorine resistance, Desal. Water Treat., 51 (2013) 6338-6345.
[49] G.V. Lowry, R.J. Hill, S. Harper, A.F. Rawle, C.O. Hendren, F. Klaessig, U. Nobbmann, P. Sayre, J. Rumble, Guidance to improve the scientific value of zeta-potential measurements in nanoEHS, Environ. Sci.: Nano, 3 (2016) 953-965.
[50] D.G. Barrett, T.S. Sileika, P.B. Messersmith, Molecular diversity in phenolic and polyphenolic precursors of tannin-inspired nanocoatings, Chem. Commun., 50 (2014) 7265-7268.
[51] C. Boo, M. Elimelech, S. Hong, Fouling control in a forward osmosis process integrating seawater desalination and wastewater reclamation, J. Membr. Sci., 444 (2013) 148-156.

[52] H.M. Hegab, Y. Wimalasiri, M.G. Markovic, L. Zou, Improving the fouling resistance of brackish water membranes via surface modification with graphene oxide functionalized chitosan, Desalination, 365 (2015) 99-107.
[53] V.M. Kochkodan, N. Hilal, V.V. Gomcharuk, L. Al-Khatib, T.I. Levadna, Effect of the surface modification of polymer membranes on their microbiological fouling, Colloid J., 68 (2006) 267-273.
[54] A.M. Turing, The chemical basis of morphogenesis, Philos. Trans. R. Soc. London, Ser. B, 237 (1952) 37-72.
[55] V.K. Vanag, I.R. Epstein, Pattern formation in a tunable medium: the Belousov-Zhabotinsky reaction in an aerosol OT microemulsion, Phys. Rev. Lett., 87 (2001) 228301-228304.
[56] A. Gierer, H. Meinhardt, A theory of biological pattern formation, Kybernetik, 12 (1972) 30-39.
[57] Z. Tan, S. Chen, X. Peng, L. Zhang, C. Gao, Polyamide membranes with nanoscale Turing structures for water purification, Science, 360 (2018) 518-521.
[58] M. Mulder, Basic Principles of Membrane Technology, Springer, Netherlands, 1996.
[59] J.G. Wijmans, R.W. Baker, The solution-diffusion model: a review, J. Membr. Sci., 107 (1995) 1-21.
[60] F.G. Donnan, Theorie der membrangleichgewichte und membranpotentiale bei vorhandensein von nicht dialysierenden elektrolyten. Ein beitrag zur physikalisch-chemischen physiologie, Z. Elektrochem. Angew. Phys. Chem., 17 (1911) 572–581.
[61] J. Glater, S. Hong, M. Elimelech, The search for a chlorine-resistant reverse osmosis membrane, Desalination, 95 (1994) 325-345.
[62] W. Choi, J. Choi, J. Bang, J.-H. Lee, Layer-by-layer assembly of graphene oxide nanosheets on polyamide membranes for durable reverse-osmosis applications, ACS Appl. Mater. Interfaces, 5 (2013) 12510-12519.
[63] J. Jeong, J.Y. Kim, J. Yoon, The role of reactive oxygen species in the electrochemical inactivation of microorganisms, Environ. Sci. Technol., 40 (2006) 6117-6122.
[64] J. Li, G. Wang, H. Zhu, M. Zhang, X. Zheng, Z. Di, X. Liu, X. Wang, Antibacterial activity of large-area monolayer graphene film manipulated by charge transfer, Sci. Rep., 4 (2014) 4359-436.
[65] O. Akhavan, E. Ghaderi, Toxicity of graphene and graphene oxide nanowalls against bacteria, ACS Nano, 4 (2010) 5731-5736.
[66] L.C. Gerber, N. Moser, N.A. Luechinger, W.J. Stark, R.N. Grass, Phosphate starvation as an antimicrobial strategy: the controllable toxicity of lanthanum oxide nanoparticles, Chem. Commun., 48 (2012) 3869–3871.
[67] H.M. Hegab, A. El-Mekawy, L. Zou, D. Mulcahy, C.P. Saint, M.G. Markovic, The controversial antibacterial activity of graphene-based materials, Carbon, 105 (2016) 362-376.
[68] X. Xie, J. Bahnemann, S. Wang, Y. Yang, M.R. Hoffmann, Nanofiltration enable by superabsorbent polymer beads for concentrating microorganisms in water samples, Sci. Rep., 6 (2016) 1-8.